EDGE ARTICLE

Check for updates

Photovoltaic-driven stable electrosynthesis of H₂O₂ in simulated seawater and its disinfection application†

Yichan Wen, [a] Youyou Feng,[b] Jing Wei, [*b] Ting Zhang,[a] Chengcheng Cai,[a] Jiyi Sun,[a] Xufang Qian [*a] and Yixin Zhao [*a]

Electrosynthesis of H₂O₂ through O₂ reduction in seawater provides bright sight on the H₂O₂ industry, which is a prospective alternative to the intensively constructed anthraquinone process. In this work, a photovoltaic-driven flow cell system is built for the electrosynthesis of H₂O₂ in simulated seawater using N-doped carbon catalysts. The N-doped carbon catalysts with multiple N-doped carbon defects can achieve a record-high H₂O₂ production rate of 34.7 mol $g_{catalyst}^{-1}$ h^{-1} under an industrially relevant current density of 500 mA cm^{-2} and a long-term stability over 200 h in simulated seawater (0.5 M NaCl). When driven by the photovoltaic system, a H₂O₂ solution of ∼1.0 wt% in 0.5 M NaCl is also obtained at about 700 mA cm^{-2}. The obtained solution is applied for disinfection of mouse wounds, with a removal rate of 100% for *Escherichia coli* and negligible toxicity to living organisms. It provides bright prospects for large-scale on-site H₂O₂ production and on-demand disinfection.

Introduction

As a green reagent and potential energy carrier, hydrogen peroxide (H₂O₂) is widely used in semiconductors, chemical industries, environmental remediation and various medical applications.[1–3] The global H₂O₂ market size had reached US$ 3.3 Billion in 2023 and will reach US$ 4.5 billion by 2032 at a growth rate of 3.3%.[4] At present, the H₂O₂ is mainly produced by an energy-intensive anthraquinone process, which is a multistep technology with high costs of storage and transportation.[5] With the development of sustainable energy, the photo/electro-chemical technology in terms of easy and distributed construction provides a broad perspective.[6–10] It also helps to prevent the risk and cost of H₂O₂ storage and transportation by on-site production.[11,12] In particular, the electro-production of H₂O₂ through a 2e⁻ ORR process provides a promising alternative to the anthraquinone process.[13–15] Considering up to 95% of H₂O₂ is applied as pure aqueous solution, the electrosynthesis of H₂O₂ should be neutral or even salt free.[4,16] Pure H₂O₂ aqueous solution production by solid-state electrolyte (SSE) cells has been developed.[6]

As the most earth-abundant resource, seawater has been considered intensively in electrocatalysis fields.[17,18] To further reduce the cost of H₂O₂ electroproduction and broaden it along the coast, using seawater as the electrolyte is a powerful strategy. Nevertheless, the exploitation of seawater mediated H₂O₂ production is still in its early stages. Unlike traditional strong acidic or alkaline electrolytes (such as H₂SO₄, HClO₄ or KOH, NaOH), seawater rich in NaCl is also bio-friendly.[19,20] Marine ranching, the rearing of fish and shellfish under artificially controlled conditions to restock the sea has developed rapidly.[21,22] However, the indiscriminate use of some drugs has led to a gradual decline in the immune and disease resistance of farmed fish.[23] In addition, the problem of diseases is becoming increasingly serious. As a substitute reagent, H₂O₂ can effectively kill water mold, bacteria, and parasites that parasitize fish and eggs, without polluting the environment unlike malachite green and formaldehyde.[24] Thus, employing seawater as the electrolyte for producing H₂O₂ can open the possibility of a straightforward use of on-site synthesized H₂O₂ in disinfection applications. Moreover, the Cl⁻ in seawater may inevitably block the active sites, especially those of metal-coordinated electrocatalysts, competing with the adsorption of oxygen on the active sites thus inhibiting the 2e⁻ ORR process.[20,25]

Among the various candidates of electrocatalysts, metal-free carbon-based materials are promising for industry-relevant production because of their tunable properties and abundance.[26–28] Carbon-based materials have exhibited excellent selectivity and productivity for H₂O₂ electrosynthesis both in acid and alkaline conditions.[29–31] Moreover, they can alleviate the shielding effect of Cl⁻ adsorption. Nevertheless,

[a]*School of Environmental Science and Engineering, Frontiers Science Center for Transformative Molecules, Shanghai Jiao Tong University, Shanghai 200240, P. R. China*

[b]*Institute of Analytical Chemistry and Instrument for Life Science, The Key Laboratory of Biomedical Information Engineering of Ministry of Education, School of Life Science and Technology, Xi'an Jiaotong University, Xi'an, 710049, P. R. China*

† Electronic supplementary information (ESI) available. See DOI: https://doi.org/10.1039/d4sc05909c

carbonaceous catalysts were limited by their low activity under neutral conditions.[20] Especially, it is still a big challenge for catalysts that operate in neutral, such as seawater at industrial scale current density in the electrosynthesis of H_2O_2. Generally, the local electronic density in the π–π conjunction structure of metal-free carbon-based catalysts is adjusted by doping heteroatoms (such as O,[32,33] N,[34,35] B[36,37] and S[38]). In recent years, N-doped carbon-based catalysts have attracted considerable attention due to their contribution in catalytic activity, selectivity and stability.[39] Furthermore, some studies have shown that N-doped polymer precursors, such as resins, performed with a high activity and stability for $2e^-$ ORR.[40–44] The pyrrole structure has been proven to be the key to the $2e^-$ ORR reactions, which were obtained by adjusting the proportion of nitrogen precursors and calcination temperature.[40,42] The N-doped sites have shown great influence on the performance of electrosynthesis of H_2O_2 due to the varied microenvironments around the catalytic sites induced by the flexible electronic structures and surface groups of N-doped carbon-based catalysts.

Herein, metal-free N-doped carbon catalysts with multiple N-doped sites were synthesized and used for electrosynthesis of H_2O_2. The optimal catalyst exhibits excellent $2e^-$ ORR performance in simulated seawater (0.5 M NaCl) electrolyte. A record high H_2O_2 production rate of 34.7 mol $g_{catalyst}^{-1}$ h^{-1} is achieved in 0.5 M NaCl. A long-term synthesis over 200 h under an industry-relevant current density of 500 mA cm^{-2} is successfully conducted. Moreover, a H_2O_2 solution of ~1.0 wt% in 0.5 M NaCl is also obtained at about 700 mA cm^{-2} when driven by the photovoltaic system. The obtained solution is applied *in situ* for disinfection of mouse wounds, with a removal rate of 100% for *Escherichia coli*, and shows negligible toxicity to living organisms. This work provides a bright prospect in large-scale on-site H_2O_2 production for emergency disinfection application.

Results and discussion

Preparation and characterizations of N-doped carbon catalysts

The metal-free N-doped carbon-based catalysts were prepared by a sequential assembly polymerization and carbonization as illustrated in Fig. 1a. Specifically, the melamine and formaldehyde were utilized to polymerize into a soluble tricarboxymethyl melamine resin, in which a triblock copolymer F127 acted as the cross-linked template. Significantly, we found that the annealing temperature is the formation hinge of the chemical structure, such as nitride, graphitic, pyridinic, pyrrolic and porphyrin N-carbon in the material. The above melamine resins were annealed in a temperature range of 400–700 °C under a N_2 atmosphere. The obtained N-doped carbon catalysts were denoted as NC400, NC500, NC600 and NC700. Details of the preparation can be found in the Experimental of ESI.†

The scanning electron microscopy (SEM) images indicate that the obtained N-doped carbon catalyst presents a typical morphology of porous carbon materials (Fig. S1a†). The N_2 adsorption–desorption isotherm shows the BET surface area of NC600 is 167.5 m^2 g^{-1}, and the pore volume is 0.3 m^3 g^{-1}
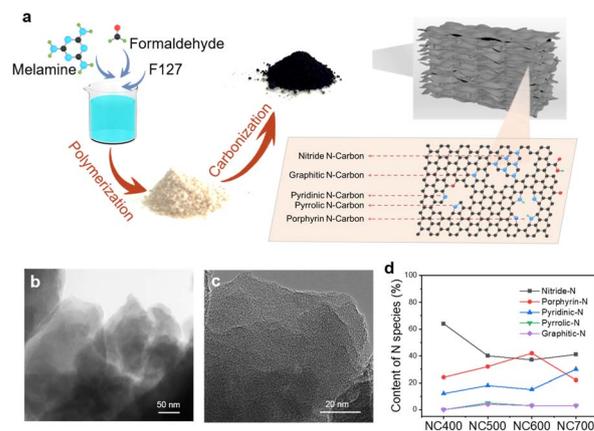

Fig. 1 (a) Synthesis and structural illustration of N-doped carbon catalysts; (b) TEM and (c) HRTEM images of NC600; (d) the nitrogen species content calculated by fitting the XPS peaks of N-doped carbon catalysts.

(Fig. S1b†). The transmission electron microscopy (TEM) image of NC600 shows a layered structure (Fig. 1b). The high-resolution TEM (HRTEM) image shows an amorphous structure of NC600, suggesting it has abundant carbon defects in NC600 (Fig. 1c). The Raman spectra with an I_D/I_G of 1.9 jointly demonstrates the short-range order of NC600 (Fig. S1c†). The peaks at 1164, 1234 1548 and 1625 cm^{-1} were assigned to the stretching vibration of C–N/C=N, and the peaks at 3414 cm^{-1}, 3600–3800, 1122 and 1826 cm^{-1} were assigned to N–H, Ar–OH, C–O and C=O, respectively (Fig. S2†). The atomic chemical structures of N-doped carbon catalysts were then investigated by X-ray photoelectron spectroscopy (XPS). There are five nitrogen species in the N-doped carbon catalysts, namely nitride-N,[45,46] pyridinic-N, pyrrolic-N and porphyrin-N[47,48] (the graphitic-N sites are a minority). The atom contents of the above nitrogen species were calculated by fitting the N 1s XPS peaks (Fig. 1d). The nitride-N content decreases from 66% to 43% with the increase of calcination temperature from 400 °C to 700 °C, while the pyridinic-N and pyrrolic-N contents increase with calcination temperature. It is worth noting that the porphyrin-N content increases from 28% to 37% as the temperature rises form 400 °C to 600 °C, but decreases to 23% when the temperature rises to 700 °C.

Electrochemical performance of N-doped carbon catalysts

The electrochemical performances for the ORR were investigated in the simulated seawater (0.5 M NaCl solution) under a three-electrode system, all potentials of this work were referenced to the reversible hydrogen electrode (RHE). The rotating ring-disk electrode (RRDE) measurements were conducted to reveal the electron transfer number of ORR on different N-doped carbon catalysts. The O_2 reduction current density at a potential was characterized on a disk electrode, and the collected H_2O_2 was oxidized on a platinum ring electrode (Fig. S3 to S6†). The NC600 catalyst has the most positive onset potential of 0.64 V_{RHE} (defined as the potential at the current density of 0.1 mA cm^{-2})[20] while the onset potential of NC400,

NC500 and NC700 are 0.38 V_{RHE}, 0.39 V_{RHE} and 0.57 V_{RHE}, respectively. And NC600 displays the highest current density among the N-doped carbon catalysts at the $2e^-$ ORR potential range of $-0.2\ V_{RHE} \sim 0.6\ V_{RHE}$ (Fig. 2a). NC600 also shows the highest H_2O_2 selectivity with a faradaic efficiency ($FE_{H_2O_2}$) of 100.0% and an electron transfer number (n) around 2.0 at 0.0 V_{RHE} among all the samples (Fig. 2b and c). In addition, the NC600 has the smallest Tafel slope value, indicating the fastest kinetics and a better catalytic activity among all the samples (Fig. S7†). The electrochemically active surface areas (ECSA) of them are similar (Fig. S8 and S9†). On the whole, NC600 shows superior properties compared with those of NC400, NC500 and NC700.

The toxic effect of Cl^- brought an enormous challenge for metal-based catalysts in H_2O_2 electro-synthesis due to the strong coordination interaction with Cl^-.[20] To study the Cl^- blocking effect on electrocatalysts, control experiments of NC600 and Co-NC600 in 0.5 M NaCl and 0.5 M $NaClO_4$ were conducted. The current densities of NC600 are similar in both 0.5 M NaCl and 0.5 M $NaClO_4$, while Co-NC600 shows a relatively lower current density in 0.5 M NaCl due to a stronger adsorption of Cl^- than that of ClO_4^- on the Co (Fig. S9†). This implies that the negative shielding effect of Cl^- on the metal-free NC600 is negligible.

The H_2O_2 production performance of the N-doped carbon catalysts was further evaluated in the simulated seawater (0.5 M NaCl solution) under an H-cell system. The current densities of

NC600 and NC700 in the presence of O_2 are 43.7 mA cm^{-2} and 44.0 mA cm^{-2} at 0 V_{RHE}, respectively. They are higher than those of NC400 and NC500 (28.0 mA cm^{-2} and 28.4 mA cm^{-2} at 0.0 V_{RHE}, respectively) at the same potential (Fig. 2d). The current density with the reactant O_2 is up to 8 times higher than that with the N_2, suggesting that the electrochemical current is mainly caused by an oxygen reduction process (Fig. 2e). To investigated the optimal electrolysis conditions of H_2O_2 production, a bulk electrolysis was conducted within 1800 s at four different potentials: 035 V_{RHE}, 0.15 V_{RHE}, $-0.15\ V_{RHE}$ and $-0.35\ V_{RHE}$ (Fig. S11†). The current density of all the N-doped carbon catalysts performs steadily at 035 V_{RHE} and 0.15 V_{RHE} within half an hour. While only NC600 still performs steadily at $-0.15\ V_{RHE}$ and $-0.35\ V_{RHE}$, indicating that NC600 could maintain an excellent electrolytic stability at the relatively negative potentials. The current density of the N-doped carbon catalysts at $-0.35\ V_{RHE}$ versus time is compared. NC600 shows the highest (~72.4 mA cm^{-2}) and the most stable current density among all the samples (Fig. 2f).

Photovoltaic-driven H_2O_2 production at practical-scale currents

To investigate the industry-relevant performance of NC600 for H_2O_2 electroproduction, a triple-phase flow cell system with a separated flow of the cathode electrolyte and anode electrolyte by a proton exchange membrane (PEM) was constructed, which can minimize the mass transfer limitation caused by poorly soluble O_2. Initially, a three-electrode mode was conducted to evaluate the H_2O_2 productivity and selectivity at various potentials in a flow cell. The H_2O_2 concentration increases from 123 mmol L^{-1} to 359 mmol L^{-1} when the electrosynthesis potential decreases from 0.1 V_{RHE} to $-0.3\ V_{RHE}$ (Fig. 3a). While the $FE_{H_2O_2}$ decreases from 100% at 0.1 V_{RHE} to 83% at $-0.3\ V_{RHE}$, but it is still catch a relatively high level under neutral
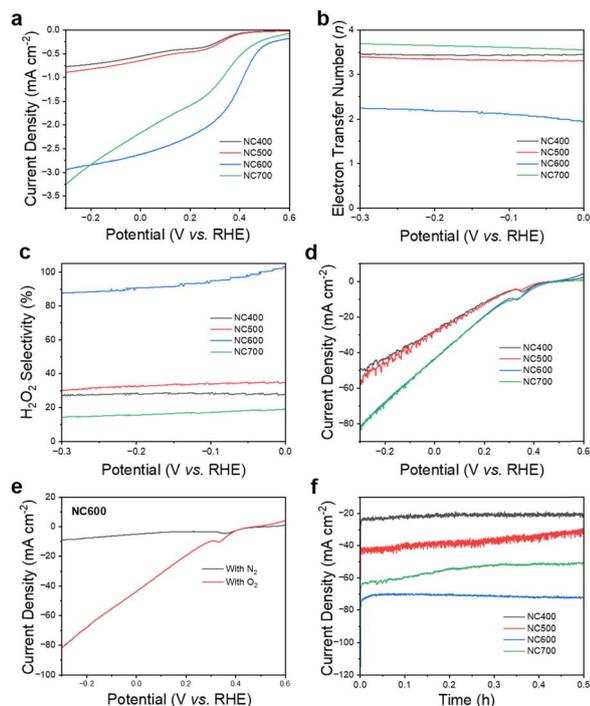

Fig. 2 (a) The RRDE LSV curves, (b) electron transfer number (n) and (c) the H_2O_2 selectivity of N-doped carbon catalysts calculated by RRDE. (d) The LSV curves of N-doped carbon catalysts, (e) the LSV curves of NC600 with and without O_2, (f) the current density varied at electrolysis time at $-0.35\ V_{RHE}$ of N-doped carbon catalysts.
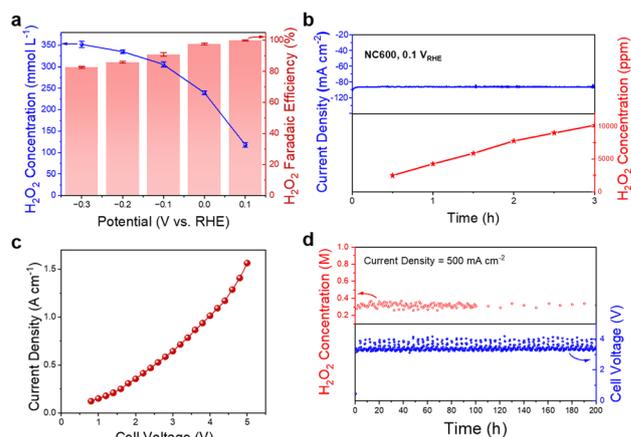

Fig. 3 The flow cell performance of NC600. (a) H_2O_2 accumulated concentration and FE at varied potentials under a three-electrode system, (b) the current density and H_2O_2 concentration at electrolysis time under a three-electrode system, (c) the LSV curve under a two-electrode system, (d) the H_2O_2 instantaneous concentration and cell voltage at 500 mA cm^{-2} varied with electrolysis time under a two-electrode system.

conditions among the reported electrocatalysts.[49] The current density remains stable within three hours of electrolysis at 0.1 V_{RHE}, and the H_2O_2 concentration accumulates up to 1 wt% (Fig. 3b). Therefore, the NC600 catalyst also exhibits an excellent performance in the flow cell, like that in RRDE and H-cells. Considering that the flow cells are assembled into stacks for a large-scale electrochemical synthesis of H_2O_2 in industrial applications, it is difficult to achieve electrolysis using a three-electrode system.[5] Therefore, the H_2O_2 electro-production performance of NC600 under the two-electrode mode is emphatically evaluated. As shown in the LSV curve, this two-electrode flow cell system can achieve a current density of ampere level when compacted in a cell voltage below 5 V without iR-correction (Fig. 3c, S12†). The stability of NC600 is investigated under a constant current density of 500 mA cm^{-2}, and the cell voltage exhibits within a 1% change over 200 h of operation (Fig. 3d). During the 200 h stability electrolysis, a continuous flow of ~1.0 wt% H_2O_2 solution with an $FE_{H_2O_2}$ of 75 ~ 95% is unceasingly produced, and a record-high H_2O_2 production rate of 34.7 mol $g_{catalyst}^{-1}$ h^{-1} was achieved.

We also investigated the effects induced by different types of ion exchange membranes on H_2O_2 production. When using anion exchange membranes (AEMs) to separate the cathode and anode chambers, the cell voltage increases from 3.2 V of PEM (Nafion® 211e) to 5.8 V, and the $FE_{H_2O_2}$ decreases to 54% (Fig. S13†). Such attenuation might be caused by the higher resistance, lower strength and poorer lifespan of AEM in comparison with the mature Nafion®, resulting in an excessively high cell voltage in an AEM cell when using an identical current density. Ultimately, this leads to a large amount of hydrogen gas emission competing with the H_2O_2 production. Thus, the current flow cell system still prefers the use of Nafion® PEM for a highly efficient H_2O_2 electroproduction.

To further reduce energy consumption and costs in the H_2O_2 electroproduction process of the NC600 catalyst, we utilized a photovoltaic device connected an energy storage battery instead of a municipal AC power to provide electricity for the flow cell system. The power of the photovoltaic device is 40 W, and its length, width, and height dimensions are 570 mm, 410 mm and 25 mm, respectively. The energy storage module, namely a lithium-ion battery with an output voltage of 5 V (Fig. S14†), was used to control the smooth output of electrical power. A xenon lamp source with an AM 1.5G filter (100 mW cm^{-2}) is used to simulate stable sunlight conditions. The schematic illustration of the photovoltaic-driven H_2O_2 electrosynthesis in simulated seawater and its on-site application in disinfection is shown in Fig. 4a. The current density of this green electricity system maintains at about 700 mA cm^{-2} within a 1% change over 3 h of operation (Fig. 4b). The H_2O_2 concentration accumulated to 0.3 mol L^{-1} (~1.0 wt%) in a 500 mL volume, and the $FE_{H_2O_2}$ only decreases from an initial 79% into 70%. The body fluids in the organism are mainly NaCl solutions, and this ~1.0 wt% concentration of H_2O_2–NaCl solution was suitable for some disinfection scenarios.

The steps to finalize an industrial process need iterative modeling of the data and a periodic adjustment of the process design before the final solution is determined and locked in to
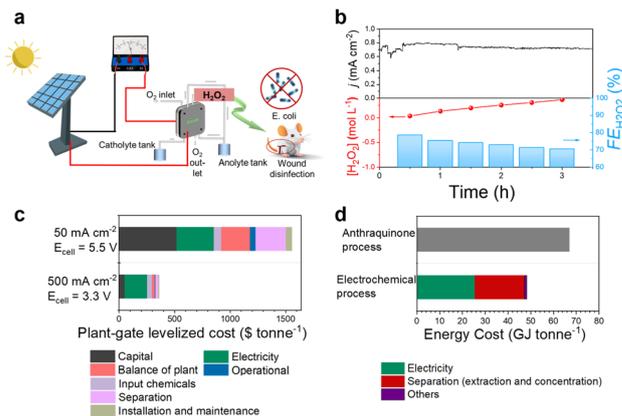

Fig. 4 (a) Illustration of an on-site photovoltaic-driven flow cell system to produce a H_2O_2 solution for sterilization, (b) the photovoltaic-driven current density, H_2O_2 accumulated concentration and faradaic efficiency at electrolysis times, (c) techno-economic analysis of H_2O_2 electrosynthesis with two different conditions and (d) energy analysis derived from two-compartment full cell results.

invest. The techno-economic and energy consumption analysis derived from the green electricity driven electrolysis system was calculated.[50,51] Recently, a plant-gate levelized H_2O_2 production consistent with capital, electricity, input chemicals, balance of plant, operational, separation, installation and maintenance cost was also designed and calculated.[52] Accordingly, we calculated the cost for H_2O_2 production under 500 mA cm^{-2}, 3.3 V and using NC600 as the electrocatalyst, and it is around US$ 360 tonne^{-1}, which is less than a third of the market price of US$ 1200 tonne^{-1} (Fig. 4c). However, when operating at the current general level of 50 mA cm^{-2} at 5.5 V, the plant-gate levelized cost climbs to US$ 1556 tonne^{-1}. The energy cost of the above plant-gate system was also calculated, which includes the costs of electricity, separation (extraction and concentration) and others. The H_2O_2 electroproduction *via* NC600 requires 48 GJ tonne^{-1} compared with 67 GJ tonne^{-1} of the anthraquinone process. Details of the parameters and calculation formula are supplied in the ESI.† This understanding of the techno-economic cost associated with diverse stages and components can directly help reduce the cost and make the process economical.

Disinfection of mice

With the increasingly uncontrolled abuse of antibiotics, more and more scientists begin to realize that we are now facing a crisis of infections for unknown drug-resistant bacterial in the future.[53] Numerous studies have shown that the presence of H_2O_2 at a concentration of 1 wt% could break down the bacterial biofilm.[54–56] As a popular medical reagent, H_2O_2 is widely used for wound disinfection with a concentration of 0.5–3.0 wt%.[57]

Herein, a growth-inhibition assay in liquid medium was utilized to evaluate the antibacterial capacity. Gram-positive *Escherichia coli* (*E. coli*) and Gram-negative *Staphylococcus aureus* (*S. aureus*) were used as models for the evaluation of the

antibacterial capacity. Three-group experiments using blank, 0.5 M NaCl and the obtained 0.3 mol L^{-1} H_2O_2 + 0.5 mol L^{-1} NaCl solution as the reagent were conducted to verify the antibacterial activity of the H_2O_2 solution produced on-site. This H_2O_2 solution decreases the viabilities of both *E. coli* and *S. aureus* cells, and significantly disturbs the survival of *E. coli* (Fig. 5a). The survival rate of *E. coli* could be down to 0% after treatment by the obtained 0.3 mol L^{-1} H_2O_2 + 0.5 mol L^{-1} NaCl solution (Fig. 5b). To investigate the morphology of bacterial changes induced by the antibacterial treatment, SEM was characterized to observe *E. coli* and *S. aureus* activity before and after H_2O_2 treatment. The *E. coli* untreated and that treated just with 0.5 mol L^{-1} NaCl solution maintained typical rod-shapes, both processed smooth and intact cell walls, which also demonstrated that this simulated seawater electrolyte exhibited little toxicity against bacteria (Fig. S15†). While since the H_2O_2 and its free radical ·OH can oxidize the lipid membrane and further damaging the bacterial membranes,[58] after treatment with the obtained 0.3 mol L^{-1} H_2O_2 + 0.5 mol L^{-1} NaCl solution, the bacterial surface became rough and wrinkled. Moreover, live/dead staining assays were conducted by using the staining kits of SYTO-9 and PI. The dead/live bacteria were marked green by SYTO 9, and the dead bacteria were marked red by PI. The control groups presented an extremely green fluorescence (dead bacteria). In contrast, the obtained 0.3 mol L^{-1} H_2O_2 + 0.5 mol L^{-1} NaCl solution treated *E. coli* groups showed a huge area of red fluorescence, indicating an outstanding antibacterial efficiency (Fig. S16†). As for *S. aureus*, the results were similar to those of *E. coli* cells but with a relatively weaker antibacterial effect. The above results indicate that the H_2O_2 solution synthesized on-site in simulated seawater has excellent disinfection effects on *E. coli*.

To investigate the antibacterial capacity of the obtained 0.3 mol L^{-1} H_2O_2 + 0.5 mol L^{-1} NaCl solution *in vivo*, mice with

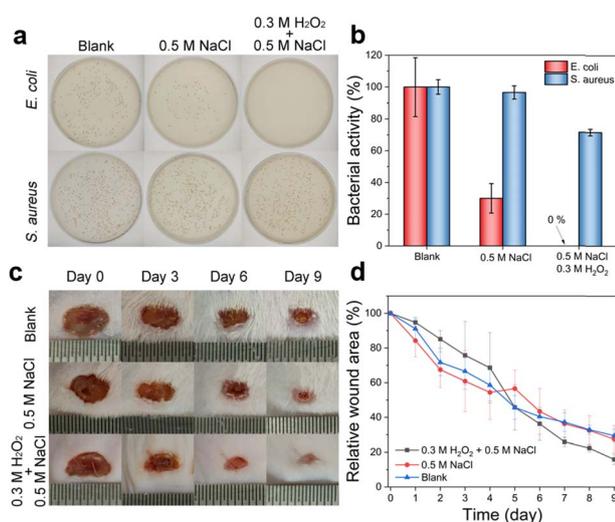Fig. 5 (a) Flat coating photos of *E. coli* and *S. aureus* treated with blank, 0.5 mol L^{-1} NaCl and the obtained 0.3 mol L^{-1} H_2O_2 + 0.5 NaCl solution, (b) the bacterial activity of the above three groups, (c) digital photos of mice wounds and (d) relative wound area over time under the above three control experiments.
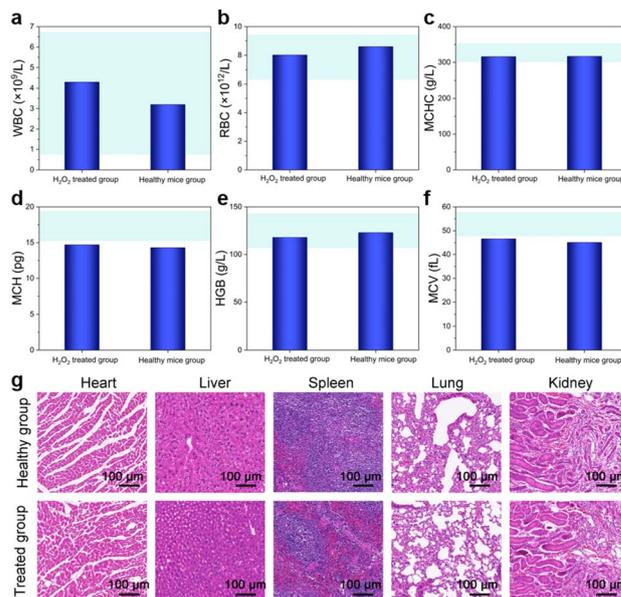

Fig. 6 Hematology analysis of mice treated with the obtained H_2O_2 solution and a healthy group. (a) WBC, (b) RBC, (c) MCHC, (d) MCH, (e) MCV, (f) HGB, (g) photomicrographs of the major organs (heart, liver, spleen, lung, and kidney, scale bar: 100 μm) stained with H&E after treatment. Results are presented as mean ± S.D. ($n = 3$).

a wound on their back were utilized as a model. The mice were also divided into three groups: treated with blank, 0.5 mol L^{-1} NaCl and the obtained 0.3 mol L^{-1} H_2O_2 + 0.5 mol L^{-1} NaCl solution on their wounds, respectively. After the reagent were injected on the back wound of the mice, photos were taken from three different groups at 72 h intervals (Fig. 5c). During the therapeutic process, the state of the wounds of the three groups were different. The wounds of mice that were treated with the obtained H_2O_2 solution rarely contained the appearance of erythema and edema over the whole process. After a 72 h therapy, the wounds of this group formed scabs, and the wound area was significantly contracted after 3 days and healed after 9 days of therapy. While the wounds of mice in the other two groups healed slowly. Consistently, the relative wound area of mice in the three groups after treatment was the smallest in the 0.3 mol L^{-1} H_2O_2 + 0.5 mol L^{-1} NaCl group (Fig. 5d).

Moreover, a series of toxic and histological analysis on the wound were conducted to further evaluate wound healing. The mice were also divided into four groups: healthy, treated with blank, 0.5 mol L^{-1} NaCl and the obtained 0.3 mol L^{-1} H_2O_2 + 0.5 mol L^{-1} NaCl solution on their wounds, respectively. The changes in mice body weight of the four groups were synchronous, suggesting the obtained 0.3 mol L^{-1} H_2O_2 + 0.5 mol L^{-1} NaCl solution showed no negative impact on weight of mice (Fig. S17†). H&E staining data also showed the wound situation of the obtained H_2O_2 solution group was almost healed and without any tissue damage (Fig. S18†).

Furthermore, to prevent the toxicity of disinfectants to the organs, we conducted hematology analysis and staining of major organs (heart, liver, spleen, lung, and kidney) with hematoxylin and eosin (H&E) on healthy mice and H_2O_2

solution treated mice. The index in mice blood of the white blood cells (WBCs), red blood cells (RBC), mean corpuscular hemoglobin concentration (MCHC), mean corpuscular hemoglobin (MCH), mean corpuscular volume (MCV), hemoglobin (HGB), platelets (PLT), platelet distribution width (PDW), lymphocyte count (LY), albumin (ALB), alkaline phosphatase (ALP), alanine aminotransferase (ALT), aspartate aminotransferase (AST), creatinine (CREA) and uric acid (UA) were all within the normal range compared with those of the heathy group (Fig. 6a–f, S19 and S20†). And the H_2O_2 solution treated group had negligible biological toxicity to organs such as the heart, liver, spleen, lungs and kidneys (Fig. 6g). In brief, the obtained H_2O_2 solution synthesized on-site in simulated seawater has excellent disinfection effects on *E. coli* and wound therapy capacity without any tissue or organ damage.

Conclusions

In summary, the N-doped carbon catalysts with strong polymer substrates have been successfully synthesized, in which various carbon defects could reduce the reaction barrier of a $2e^-$ ORR. Consequently, a record high $FE_{H_2O_2}$ of 100% among metal-free carbon-based materials under neutral conditions was obtained by the NC600 catalyst. At the device level, an industry-relevant current density of 500 mA cm^{-2} was successfully achieved in simulated seawater (0.5 mol L^{-1} NaCl) during a long-term operation of 200 h. A record high H_2O_2 production rate of 34.7 mol g$_{cat}^{-1}$ h^{-1} with a record $FE_{H_2O_2}$ of 93.0% under neutral conditions was achieved. Furthermore, a photovoltaic-driven seawater-induced H_2O_2 electroproduction system was constructed and a ~1.0 wt% H_2O_2 in simulated seawater was produced. This H_2O_2 solution synthesized on-site has excellent disinfection effects on *E. coli* and wound therapy capacity without any tissue or organ damage. We hope that this strategy of photovoltaic-driven seawater-induced H_2O_2 electroproduction by metal-free N-doped carbon catalysts can shed light on the low-cost and longevity H_2O_2 production and its on-site application.

Ethical statement

All animal procedures were performed in accordance with the Guidelines for Care and Use of Laboratory Animals of Xi'an Jiaotong University and approved by the Animal Ethics Committee of Xi'an Jiaotong University.

Data availability

Data are available on request from the authors.

Author contributions

Y. Z., X. Q. and J. W. designed and directed the research. Y. W. and Y. F. carried out the catalyst fabrications and characterizations as well as data analysis. T. Z., C. C. and J. S. participated in the characterization and manuscript revision. Y. Z., X. Q. and Y. W. wrote the manuscript with input from all authors.

Conflicts of interest

There are no conflicts to declare.

Acknowledgements

References

1 S. Siahrostami, A. Verdaguer-Casadevall, M. Karamad, D. Deiana, P. Malacrida, B. Wickman, M. Escudero-Escribano, E. A. Paoli, R. Frydendal, T. W. Hansen, I. Chorkendorff, I. E. L. Stephens and J. Rossmeisl, *Nat. Mater.*, 2013, **12**, 1.

2 Z. W. Seh, J. Kibsgaard, C. F. Dickens, I. B. Chorkendorff, J. K. Norskov and T. F. Jaramillo, *Science*, 2017, **355**, 1.

3 N. Wang, S. B. Ma, R. Y. Zhang, L. F. Wang, Y. A. Wang, L. H. Yang, J. H. Li, F. Guan, J. Z. Duan and B. R. Hou, *Advanced Science*, 2023, **10**, 11.

4 IMARC Group, *Hydrogen Peroxide Market Report by Application (Chemical Synthesis, Bleaching, Disinfectant, Cleaning and Etching, and Others), End-Use (Pulp and Paper, Food and Beverages, Water Treatment, Textiles and Laundry, Oil and Gas, Healthcare, Electronics, and Others), and Region 2024-2032*, 2023.

5 Y. Wen, T. Zhang, J. Wang, Z. Pan, T. Wang, H. Yamashita, X. Qian and Y. Zhao, *Angew. Chem., Int. Ed.*, 2022, **61**, e202205972.

6 C. Xia, Y. Xia, P. Zhu, L. Fan and H. Wang, *Science*, 2019, **366**, 226–231.

7 S. Siahrostami, A. Verdaguer-Casadevall, M. Karamad, D. Deiana, P. Malacrida, B. Wickman, M. Escudero-Escribano, E. A. Paoli, R. Frydendal, T. W. Hansen, I. Chorkendorff, I. E. L. Stephens and J. Rossmeisl, *Nat. Mater.*, 2013, **12**, 1137–1143.

8 J. J. Gao, H. B. Yang, X. Huang, S. F. Hung, W. Z. Cai, C. M. Jia, S. Miao, H. M. Chen, X. F. Yang, Y. Q. Huang, T. Zhang and B. Liu, *Chem*, 2020, **6**, 658–674.

9 H. Yu, F. T. Zhang, Q. Chen, P. K. Zhou, W. D. Xing, S. B. Wang, G. G. Zhang, Y. Jiang and X. Chen, *Angew. Chem., Int. Ed.*, 2024, **136**, e202402297.

10 D. D. Zheng, Y. H. Wu, X. T. Yang, S. B. Wang and Y. X. Fang, *Chemsuschem*, 2024, **17**, e202400528.

11 X. Y. Guo, S. R. Lin, J. X. Gu, S. L. Zhang, Z. F. Chen and S. P. Huang, *ACS Catal.*, 2019, **9**, 11042–11054.

12 S. Y. Chen, T. Luo, K. J. Chen, Y. Y. Lin, J. W. Fu, K. Liu, C. Cai, Q. Y. Wang, H. J. W. Li, X. Q. Li, J. H. Hu, H. M. Li, M. S. Zhu and M. Liu, *Angew. Chem., Int. Ed.*, 2021, **60**, 16607–16614.

13 E. E. Kalu and C. Oloman, *J. Appl. Electrochem.*, 1990, **20**, 932–940.

14 K. Otsuka and I. Yamanaka, *Electrochim. Acta*, 1990, **35**, 319–322.

15 T. Iwasaki, Y. Masuda, H. Ogihara and I. Yamanaka, *Electrocatalysis*, 2018, **9**, 236–242.

16 X. Zhang, Y. Xia, C. Xia and H. T. Wang, *Trends Chem.*, 2020, **2**, 942–953.

17 J. X. Guo, Y. Zheng, Z. P. Hu, C. Y. Zheng, J. Mao, K. Du, M. Jaroniec, S. Z. Qiao and T. Ling, *Nat. Energy*, 2023, **8**, 264–272.

18 H. P. Xie, Z. Y. Zhao, T. Liu, Y. F. Wu, C. Lan, W. C. A. Jiang, L. Y. Zhu, Y. P. Wang, D. S. Yang and Z. P. Shao, *Nature*, 2022, **612**, 673–678.

19 H. Huang, F. M. Li, Q. Xue, Y. Zhang, S. W. Yin and Y. Chen, *Small*, 2019, **15**, 11.

20 Q. L. Zhao, Y. Wang, W. H. Lai, F. Xiao, Y. X. Lyu, C. Z. Liao and M. H. Shao, *Energy Environ. Sci.*, 2021, **14**, 5444–5456.

21 X. J. Zhou, X. Zhao, S. Y. Zhang and J. Lin, *Water*, 2019, **11**, 27.

22 D. M. Bartley, Bergen, Norway, 1997.

23 G. James, P. P. Geetha, S. T. Puthiyedathu and R. K. V. Jayadradhan, *3 Biotech*, 2023, **13**, 13.

24 M. G. Bondad-Reantaso, B. MacKinnon, I. Karunasagar, S. Fridman, V. Alday-Sanz, E. Brun, M. Le Groumellec, A. H. Li, W. Surachetpong, I. Karunasagar, B. Hao, A. Dall'Occo, R. Urbani and A. Caputo, *Rev. Aquac.*, 2023, **15**, 1421–1451.

25 J. Yu, B. Q. Li, C. X. Zhao and Q. Zhang, *Energy Environ. Sci.*, 2020, **13**, 3253–3268.

26 L. L. Cui, B. Chen, L. S. Zhang, C. He, C. Shu, H. Y. Kang, J. Qiu, W. H. Jing, K. Ostrikov and Z. H. Zhang, *Energy Environ. Sci.*, 2024, **17**, 655–667.

27 G. F. Han, F. Li, W. Zou, M. Karamad, J. P. Jeon, S. W. Kim, S. J. Kim, Y. F. Bu, Z. P. Fu, Y. L. Lu, S. Siahrostami and J. B. Baek, *Nat. Commun.*, 2020, **11**, 9.

28 L. Han, Y. Y. Sun, S. Li, C. Cheng, C. E. Halbig, P. Feicht, J. L. Hübner, P. Strasser and S. Eigler, *ACS Catal.*, 2019, **9**, 1283–1288.

29 C. Zhang, W. Q. Shen, K. Guo, M. Xiong, J. Zhang and X. Lu, *J. Am. Chem. Soc.*, 2023, **145**, 11589–11598.

30 X. Zhang, X. H. Zhao, P. Zhu, Z. Adler, Z. Y. Wu, Y. Y. Liu and H. T. Wang, *Nat. Commun.*, 2022, **13**, 11.

31 S. C. Perry, D. Pangotra, L. Vieira, L. I. Csepei, V. Sieber, L. Wang, C. P. de León and F. C. Walsh, *Nat. Rev. Chem*, 2019, **3**, 442–458.

32 Z. Y. Lu, G. X. Chen, S. Siahrostami, Z. H. Chen, K. Liu, J. Xie, L. Liao, T. Wu, D. C. Lin, Y. Y. Liu, T. F. Jaramillo, J. K. Norskov and Y. Cui, *Nat. Catal.*, 2018, **1**, 156–162.

33 K. Jiang, S. Back, A. J. Akey, C. Xia, Y. F. Hu, W. T. Liang, D. Schaak, E. Stavitski, J. K. Norskov, S. Siahrostami and H. T. Wang, *Nat. Commun.*, 2019, **10**, 11.

34 T. P. Fellinger, F. Hasche, P. Strasser and M. Antonietti, *J. Am. Chem. Soc.*, 2012, **134**, 4072–4075.

35 D. Iglesias, A. Giuliani, M. Melchionna, S. Marchesan, A. Criado, L. Nasi, M. Bevilacqua, C. Tavagnacco, F. Vizza, M. Prato and P. Fornasiero, *Chem*, 2018, **4**, 106–123.

36 A. G. Saputro, A. K. Fajrial, A. L. Maulana, F. Fathurrahman, M. K. Agusta, F. T. Akbar and H. K. Dipojono, *J. Phys. Chem. C*, 2020, **124**, 11383–11391.

37 Y. Xia, X. H. Zhao, C. Xia, Z. Y. Wu, P. Zhu, J. Y. T. Kim, X. W. Bai, G. H. Gao, Y. F. Hu, J. Zhong, Y. Y. Liu and H. T. Wang, *Nat. Commun.*, 2021, **12**, 12.

38 Y. Y. Meng, D. Voiry, A. Goswami, X. X. Zou, X. X. Huang, M. Chhowalla, Z. W. Liu and T. Asefa, *J. Am. Chem. Soc.*, 2014, **136**, 13554–13557.

39 K. P. Gong, F. Du, Z. H. Xia, M. Durstock and L. M. Dai, *Science*, 2009, **323**, 760–764.

40 W. Peng, J. Liu, X. Liu, L. Wang, L. Yin, H. Tan, F. Hou and J. Liang, *Nat. Commun.*, 2023, **14**, 4430.

41 Z. M. Yang, L. G. Feng, Y. Y. Pang and G. L. Chai, *Catal. Lett.*, 2024, **154**(9), 4023–4031.

42 L. Jing, Q. Tian, W. Wang, X. Li, Q. Hu, H. Yang and C. He, *Adv. Energy Mater.*, 2024, **17**, 2304418.

43 Q. Tian, L. Y. Jing, H. N. Du, Y. C. Yin, X. L. Cheng, J. X. Xu, J. Y. Chen, Z. X. Liu, J. Y. Wan, J. Liu and J. L. Yang, *Nat. Commun.*, 2024, **15**, 14.

44 Y. Y. Sun, I. Sinev, W. Ju, A. Bergmann, S. Dresp, S. Kühl, C. Spöri, H. Schmies, H. Wang, D. Bernsmeier, B. Paul, R. Schmack, R. Kraehnert, B. Roldan Cuenya and P. Strasser, *ACS Catal.*, 2018, **8**, 2844–2856.

45 M. O. Azeez, A. Tanimu, K. Alhooshani and S. A. Ganiyu, *Arabian J. Chem.*, 2022, **15**, 15.

46 J. S. Nam, A. R. Kim, D. M. Kim, T. S. Chang, B. S. Kim and J. W. Bae, *Catal. Commun.*, 2017, **99**, 141–145.

47 H. Yamashige, S. Matsuo, T. Kurisaki, R. C. C. Perera and H. Wakita, *Anal. Sci.*, 2005, **21**, 635–639.

48 A. Ghosh, J. Moulder, M. Bröring and E. Vogel, *Angew. Chem., Int. Ed.*, 2001, **40**, 431–434.

49 Y. F. Bu, Y. B. Wang, G. F. Han, Y. X. Zhao, X. L. Ge, F. Li, Z. H. Zhang, Q. Zhong and J. B. Baek, *Adv. Mater.*, 2021, **33**, 19.

50 X. Li, J. Y. Wang, T. Zhang, T. F. Wang and Y. X. Zhao, *ACS Sustainable Chem. Eng.*, 2022, **10**, 9546–9552.

51 J. Y. Wang, X. Li, M. L. Wang, T. Zhang, X. Y. Chai, J. L. Lu, T. F. Wang, Y. X. Zhao and D. Ma, *ACS Catal.*, 2022, **12**, 6722–6728.

52 B.-H. Lee, H. Shin, A. S. Rasouli, H. Choubisa, P. Ou, R. Dorakhan, I. Grigioni, G. Lee, E. Shirzadi, R. K. Miao, J. Wicks, S. Park, H. S. Lee, J. Zhang, Y. Chen, Z. Chen, D. Sinton, T. Hyeon, Y.-E. Sung and E. H. Sargent, *Nat. Catal.*, 2023, **6**, 234–243.

53 B. Aslam, W. Wang, M. I. Arshad, M. Khurshid, S. Muzammil, M. H. Rasool, M. A. Nisar, R. F. Alvi, M. A. Aslam, M. U. Qamar, M. K. F. Salamat and Z. Baloch, *Infect. Drug Resist.*, 2018, **11**, 1645–1658.

54 L. Z. Gao, K. M. Giglio, J. L. Nelson, H. Sondermann and A. J. Travis, *Nanoscale*, 2014, **6**, 2588–2593.

55 A. E. K. Loo, Y. T. Wong, R. J. Ho, M. Wasser, T. H. Du, W. T. Ng and B. Halliwell, *PLoS One*, 2012, **7**, 13.

56 E. Hayashi, T. Mokudai, Y. Yamada, K. Nakamura, T. Kanno, K. Sasaki and Y. Niwano, *J. Biosci. Bioeng.*, 2012, **114**, 193–197.

57 E. Schültke, J. A. Hampl, L. Jatzwauk, D. Krex and G. Schackert, *Acta Neurochir.*, 1999, **141**, 525–528.

58 N. G. Durmus, E. N. Taylor, K. M. Kummer and T. J. Webster, *Adv. Mater.*, 2013, **25**, 5706–5713.